

Specific heat in different magnetic phases of $R\text{Ni}_2\text{B}_2\text{C}$ ($R = \text{Gd}, \text{Ho}, \text{Er}$): theory and experiment

M. ElMassalami and R. M. Saeed, C. M. Chaves

Instituto de Fisica-UFRJ, CxP 68528, 21941-972, Rio de Janeiro, Brazil

H. Takeya,

National Institute for Materials Science,

1-2-1 Sengen, Tsukuba, Ibaraki, 305-0047, Japan

M. Doerr

Institut für Festkörperphysik, Technische Universität Dresden, D-01062 Dresden, Germany

H. Michor

Institut für Festkörperphysik, Technische Universität Wien, A-1040 Wien, Austria

M. Rotter

University of Oxford, Department of Physics

Clarendon Laboratory, Parks Road Oxford OX1 3PU

(Dated: November 20, 2018)

Abstract

The borocarbides $R\text{Ni}_2\text{B}_2\text{C}$ ($R=\text{Gd}, \text{Ho}, \text{Er}$) exhibit a large variety of magnetic states and as a consequence rich phase diagrams. We have analyzed the nature of these states by specific heat investigations. The data were measured down to 0.5 K and up to 80 kOe. The overall evolution of each $C_{mag}(T, H)$ curve is observed to reflect faithfully the features of the corresponding $H - T$ phase diagram. Within the lower ranges of temperature and fields, the calculations based on linearized field-dependent spin-wave theory are found to reproduce satisfactorily the measured $C_{mag}(T, H)$ curves: accordingly, within these ranges, the thermodynamical properties of these compounds can be rationalized in terms of only two parameters: the spin-wave energy gap and the stiffness coefficient. For the intermediate fields ranges ($H_1 < H < H_{sat}$) wherein successive field-induced metamagnetic modes are stabilized, the evolution of $C_{mag}(T, H)$ is discussed in terms of the Maxwell relation $(\partial C_{mag}/\partial H)_T = T (\partial^2 M/\partial T^2)_H$. For the particular case of $\text{GdNi}_2\text{B}_2\text{C}$ wherein the anisotropy is dictated by the classical dipole interaction, $C_{mag}(T, H)$ across the whole ordered state is numerically evaluated within the model of Jensen and Rotter [PRB **77** (2008) 134408].

PACS numbers:

I. INTRODUCTION

The $H-T$ magnetic phase diagrams of the heavy members of the intermetallic $R\text{Ni}_2\text{B}_2\text{C}$ (R = rare earth) magnets are characterized by a cascade of metamagnetic transformations, higher Neel points T_N , and stronger saturation fields, H_{sat} (see Refs.1, 2 and references therein). Both T_N and H_{sat} are well scaled by de Gennes factors testifying to the involvement of the indirect exchange coupling mechanism.³ Moreover, except for $\text{GdNi}_2\text{B}_2\text{C}$, there are strong anisotropic forces and the competition between these forces and the exchange interaction is one of the main driving mechanism behind the characteristic features of their magnetic phase diagrams.^{1,2} In general, the role of these competing forces is analyzed in terms of a Hamiltonian that consists of bilinear exchange, single-ion crystalline electric field (CEF), and dipolar interactions.^{4,5,6} Calculations based on such a Hamiltonian yield $H-T$ phase diagrams that are in reasonable agreement with experiments on, say, $\text{HoNi}_2\text{B}_2\text{C}$,^{4,5} $\text{GdNi}_2\text{B}_2\text{C}$,^{7,8}, and $\text{ErNi}_2\text{B}_2\text{C}$.⁶

The zero-field magnetic structures of the $R\text{Ni}_2\text{B}_2\text{C}$ compounds can be divided into two broad classes:⁹ (i) the equal-amplitude, collinear, and commensurate AFM structures (R =Pr, Nd, Dy, Ho): here the moments are coupled ferromagnetically within the layers which are, in turn, antiferromagnetically stacked on each other along the c axis and (ii) the amplitude-modulated, incommensurate structures (R = Gd , Tb, Er, Tm); on lowering the temperature, these modulated structures are gradually transformed into an equal-amplitude, squared-up spin-density states.

On applying an external magnetic field along the easy-axis, both the commensurate and incommensurate magnetic modes are observed to undergo a cascade of magnetic phase transformations leading to a set of different magnetic modes; each having a distinct propagation vector and a distinct total magnetic moment. For the case of, say, $\text{HoNi}_2\text{B}_2\text{C}$ and $\text{ErNi}_2\text{B}_2\text{C}$, there emerges a very rich and interesting $H-T$ magnetic phase diagram^{10,11,12} with characteristic features that are reflected in all measured thermodynamical properties. As an example, the low-temperature magnetization isotherms show a cascade of step-like metamagnetic phase transformations with constant plateau between the consecutive transformations.^{13,14,15,16,17} As the low-temperature magnetic properties are governed by the excitation spectra of the magnon quasiparticles then, according to the spin-wave theory, the surge of such a stair-like features is a manifestation of related field-dependent distinct

features in the dispersion relations or density of states of the magnon quasiparticles. Then a detailed spin-wave analysis of the H - and T -dependence of the thermodynamical properties would contribute positively to the understanding of the magnetic phase diagrams and the related thermodynamical properties of these borocarbide magnets. Using field-dependent specific heat measurements on single-crystals of $R\text{Ni}_2\text{B}_2\text{C}$ ($R = \text{Gd}, \text{Ho}, \text{Er}$), this work investigated the magnetic contribution to the specific heat when T and H are varied across these H - T phase diagrams.

The magnetic structures of the compounds under study are well established for the high- and low-field part of the phase diagram: within the intermediate-field range, the structures are either unknown or too complex. Furthermore, it happened that the highest magnetic field available for this study is lower than the one needed to reach the high-field saturated range. Accordingly, the comparison of the measured and calculated magnetic specific heats (the latter is based on spin-wave theory) was carried out only for the lower field limit (§ II.A and IV.C). For the intermediate-field range (as well as across the available $H - T$ plane of the phase diagram), basic thermodynamical relations were employed to relate the field evolution of the measured magnetic specific heat to the thermal evolution of the isofield magnetization curves (§ II.C and § IV.C). Finally, since the linearized magnon theory is applicable only for the lower temperature range, mean-field model calculations were carried out to evaluate the magnetic specific heat within the higher range of the ordered state; this part of the study was restricted to only $\text{GdNi}_2\text{B}_2\text{C}$ (§ II.B and § IV.C.1.b): in contrast to $R = \text{Ho}$ and Er , $\text{GdNi}_2\text{B}_2\text{C}$ has negligible crystalline field anisotropy and as such the classical dipole interactions play a crucial role in shaping its magnetic structure.

II. THEORETICAL BACKGROUND

A. Field-dependent magnon specific heat of $R\text{Ni}_2\text{B}_2\text{C}$.

The magnetic properties of $R\text{Ni}_2\text{B}_2\text{C}$ are usually described in terms of the Hamiltonian:

$$\mathcal{H} = \mathcal{H}_Z + \mathcal{H}_{ex} + \mathcal{H}_{CEF}, \quad (1)$$

where \mathcal{H}_Z is the Zeeman term with the field H applied at angle θ away from the easy axis:

$$\mathcal{H}_Z = -g\mu_B \vec{H} \cdot \sum_j \vec{S}_j, \quad (2)$$

where \vec{S}_j is the total angular momentum operator of the j^{th} R^{3+} -ion, g_j is the Landé factor, and μ_B is the Bohr magneton. The bilinear isotropic exchange interaction is:

$$\mathcal{H}_{ex} = -\frac{1}{2} \sum_{ij} \mathcal{J}(ij) \vec{S}_i \cdot \vec{S}_j, \quad (3)$$

where $\mathcal{J}(ij)$ is the isotropic coupling between \vec{S}_i and \vec{S}_j . Considering the low-temperature commensurate AFM structures of $R\text{Ni}_2\text{B}_2\text{C}$ then \mathcal{H}_{ex} (Eq. 3) can be split into two terms:

$$\mathcal{H}_{ex} = + \sum_{\langle ij \rangle, L \in A, B} \mathcal{J}_{ij}^L \vec{S}_i^L \cdot \vec{S}_j^L + \sum_{\langle ij \rangle A, B} \mathcal{J}_{ij}^{AB} \vec{S}_i^A \cdot \vec{S}_j^B \quad (4)$$

\mathcal{J}_{ij}^A couples moments \vec{S}_i^L and \vec{S}_j^L within the same layer ($L = A$ or B) and \mathcal{J}_{ij}^{AB} couples moments from different layers. At lower temperatures, we assume that the net effect of \mathcal{H}_{CEF} on the magnetic moment can be approximated by an easy-axis anisotropic field (represented by \vec{H}_a),^{18,19} consequently:

$$\mathcal{H}_{CEF} + \mathcal{H}_Z = -g\mu_B(\vec{H}_a + \vec{H}) \cdot \sum_{i \in A} \vec{S}_i^A - g\mu_B(\vec{H}_a - \vec{H}) \cdot \sum_{j \in B} \vec{S}_j^B. \quad (5)$$

Let us consider the following useful simplification: as far as the magnon propagation is concerned, the low-temperature squared-up incommensurate magnetic structures is assumed to behave as if it is a collinear AFM structure (for, say, $\text{ErNi}_2\text{B}_2\text{C}$, this ignores the presence of the kinks along the a axis): such a simplification is motivated by the remarkable feature that though $R\text{Ni}_2\text{B}_2\text{C}$ ($R=\text{Ho}, \text{Er}$) have different magnetic structures,⁹ however they manifest similar stair-like features in their $M(T, H)$ isotherms^{13,14,15,16,17} as well as similar expression for their zero-field $C_{mag}(T, H)$ curves.²⁰

Using standard linearized spin-wave procedures,¹⁸ the total Hamiltonian (Eq. 1) is diagonalized and consequently the magnetic specific heat is calculated. Based on the strength of the applied field, three different situations can be distinguished: (i) the low-field limit ($H < H_{\text{sf}}$: the spin-flop field) wherein the spins are basically aligned along the preferred orientation, (ii) the intermediate field regime wherein a series of field-induced metamagnetic states are stabilized. and (iii) the high field limit ($H \geq H_{\text{sat}}$: saturated field) wherein spins are driven towards paramagnetic saturation.

1. *Low-field approximation* ($H < H_{sf}$)

The dispersion relation of the two modes (+ and -) are:

$$\begin{aligned} \hbar\omega_k^\pm &= +\sqrt{A^2 - B^2} \pm g\mu_B H \cos(\theta), \\ A &= 4S\mathcal{J}_o \{1 - 0.5 [\cos(ak_x) + \cos(ak_y)]\} + 8S\mathcal{J}_1 + g\mu_B H_a, \\ B &= 2S\mathcal{J}_1 \left\{ \cos\left(\frac{a}{2}k_x + \frac{a}{2}k_y + \frac{c}{2}k_z\right) + \cos\left(\frac{a}{2}k_x + \frac{a}{2}k_y - \frac{c}{2}k_z\right) \right. \\ &\quad \left. + \cos\left(\frac{a}{2}k_x - \frac{a}{2}k_y + \frac{c}{2}k_z\right) + \cos\left(-\frac{a}{2}k_x + \frac{a}{2}k_y + \frac{c}{2}k_z\right) \right\} \end{aligned} \quad (6)$$

where \mathcal{J}_0 and \mathcal{J}_1 are effective exchange couplings among the nearest neighboring within, respectively, the same plane and within neighboring planes. Accordingly, there are two distinct field-dependent energy gaps:

$$\Delta_a^\pm(H) = +\sqrt{(g\mu_B H_a)^2 + 16\mathcal{J}_1 g\mu_B S H_a} \pm g\mu_B H \cos(\theta) = \Delta_a \pm g\mu_B H \cos(\theta); \quad (7)$$

evidently $\Delta^\pm(H)$ do not depend on \mathcal{J}_o and their separation is linearly related to $H \cos(\theta)$.

At lower temperature where long-wave limit is valid, the integration over the allowed k -space yields the magnon specific heat:

$$\begin{aligned} C_{mag}(T, H) &= R\Delta_a^4 / (4\pi^2 D_a^3 T^2) \sum_{m=1}^{\infty} \{ T \cosh(m\xi/T) [K_4(m\Delta_a/T) + \langle 1 + 2\xi^2/\Delta_a^2 \rangle K_2(m\Delta_a/T)] \\ &\quad - 0.5m\xi \sinh(m\xi/T) [K_4(m\Delta_a/T) - K_0(m\Delta_a/T)] \} \end{aligned} \quad (8)$$

where $K_n(m\Delta_a/T)$ represents the modified Bessel function of the second kind, $\xi = g\mu_B H \cos(\theta)/k_B$ and D_a is a measure of the stiffness and is function of the exchange couplings and magnetic anisotropy:

$$D_a = (16(\mathcal{J}_0 + \mathcal{J}_1)\mathcal{J}_0 S^2 + 2\mathcal{J}_0 S(g\mu_B H_a))^{1/3} \cdot (4\mathcal{J}_1 S)^{1/3} \quad (9)$$

Due to the type of the undertaken approximations, Eq. 8 does not hold for $H \cos(\theta)$ equal or higher than the spin-flop field H_{sf} which is the value at which the lower branch goes to zero. The field influence on Eq. 8 enters only through $H \cos(\theta)$. Furthermore, this equation reduces to Eq. 25 of Joenk¹⁹ when $\mathcal{J}_0 = \mathcal{J}_1$ and it gives the well-known T^3 relation when $k_B T > \Delta_a$.¹⁸

For $T \rightarrow 0$, $\Delta_a/T \rightarrow \infty$, and $\xi < \Delta_a$, Eq. 8 reduces to:

$$C_{mag}(T, H) \simeq \frac{R\Delta_a^{7/2}}{2^{1/2}\pi^{3/2}D_a^3 T^{1/2}} \exp\left(\frac{\xi - \Delta_a}{T}\right) \left[1 - 2\frac{\xi}{\Delta_a} + \left(\frac{\xi}{\Delta_a}\right)^2 \dots \right], \quad (10)$$

indicating a dominant exponential character within this $H - T$ region.

2. *Intermediate fields range ($H_{sf} < H < H_{sat}$)*

As mentioned in § I, the absence of a detailed description of the involved magnetic structures together with the absence of analytical expression for the dispersion relations hinder any direct evaluation of the magnon specific heat contribution within this range.

3. *The high-field limit ($H > H_{sat}$)*

Due to the limitation of our experimental conditions, we were not able to probe the magnon contribution within the region of the $H - T$ phase diagram wherein the induced FM state is established. Nevertheless for completeness sake we derive the magnetic contribution for this state in appendix A below.

B. Mean-field Model calculation of $C_{mag}(T, H)$ of $\text{GdNi}_2\text{B}_2\text{C}$

The above calculations of the magnon $C_{mag}(T, H)$ of $\text{RNi}_2\text{B}_2\text{C}$ compounds are valid only within the lower temperature range, mostly below liquid helium temperatures. To investigate the magnetic contribution within the whole magnetically ordered range, we resort to mean-field model calculations applied on the simpler case of the ordered $7/2S$ -moments of $\text{GdNi}_2\text{B}_2\text{C}$. Jensen and Rotter⁸ showed that a model consisting of a sum of the bilinear Heisenberg exchange term and the classical dipole interaction is able to explain the features of the whole magnetic phase diagram as well as the so-called magnetoelastic paradox.²¹ and the zero-field $C_{mag}(T)$ of $\text{GdNi}_2\text{B}_2\text{C}$. here, in this work, their calculations of $C_{mag}(T, H)$ are extended to fields up to $H \leq 80$ kOe using the McPhase program package (www.mcphase.de).²²

C. Application of the Maxwell relation to correlate $M(T, H)$ and $C_{mag}(T, H)$

An applied field on an AFM mode tends to remove the degeneracy appearing in Eqs. 6 and 7. As a consequence, the fractional contribution of the lower mode to $C_{mag}(T, H)$ increases leading to $(\partial C_{mag}/\partial H)_T > 0$. On the other hand, for $H \rightarrow H_{sat}$, an increase in H would induce a gradual decrease in $C_{mag}(T, H)$ resulting in $(\partial C_{mag}/\partial H)_T < 0$. Similar arguments hold for $M(T, H)$. In fact the following Maxwell equations relate the evolution

of $M(T, H)$ to that of $C_{mag}(T, H)$:

$$(\partial S_{mag}/\partial H)_T = (\partial M/\partial T)_H \quad (11a)$$

$$(\partial C_{mag}/\partial H)_T = T (\partial^2 M/\partial T^2)_H. \quad (11b)$$

These general relations are very helpful in the analysis of $S_{mag}(T, H)$ and $C_{mag}(T, H)$ since it is much easier to measure the thermal evolution of $M(T, H)$ than the field dependence of $C_{mag}(T, H)$. Furthermore, they hold across the whole $H - T$ phase diagram and are independent of field orientation (whether $H||a$ or $H||c$) or the type of the involved magnetic structure (whether commensurate or incommensurate). This utility is most welcomed when investigating those regions of the $H - T$ phase diagrams wherein the spin-wave analysis of § II.A is not applicable.

Evidently each of $C_{mag}(T < T_N, H)$ and $M(T < T_N, H)$ would mirror the exotic features of the $H - T$ phase diagrams of RNi_2B_2C ;^{13,14,15,16,16} in fact, these diagrams have been constructed from the magnetic anomalies occurring in $C_{mag}(T < T_N, H)$ and $M(T < T_N, H)$ as well as many other magnetic properties such as the integrated intensities of the magnetic neutron diffractograms;^{10,11} the magnetostriction,^{17,23} and the magnetoresistivity.^{24,25} Here in this work, we use Eqs. 11a and 11b to discuss the general trend of $C_{mag}(T, H)$ in terms of the trend of the extensively reported $M(T, H)$ curves.¹

III. EXPERIMENTAL

The RNi_2B_2C ($R = \text{Gd, Ho, Er}$) single-crystals were selected for this study because they offer a good representation of the magnetic properties of the whole RNi_2B_2C series: $HoNi_2B_2C$ is a typical representative of the collinear, commensurate, AFM structures while $ErNi_2B_2C$ and $GdNi_2B_2C$ are good representatives of the modulated, incommensurate magnetic structures; the anisotropic forces are stronger in the former²⁶ while extremely weaker in the latter.^{23,27} $GdNi_2B_2C$ has negligible CEF forces; nonetheless, it is shown that the dipolar forces are essential for directing the moments transversal to the propagation vector $(0.55, 0, 0)$.⁷

The single crystals of these three representatives, together with that of the reference YNi_2B_2C , were grown by floating zone method.²⁸ Results from extensive structural and physical characterizations are in good agreement with the reported data, confirming the

good quality of our crystals. The temperature-dependent specific heat at fixed fields was measured on two different setups. One is pulse-type adiabatic calorimeter [500 mK $<T<$ 25 K, 120 kOe] and the second is a quasi-adiabatic setup with a temperature range covering 1.5-100K and a field up to 80 kOe. For the sake of completeness, we quote some of our results (in particular the zero-field magnetic specific heat) that had been reported in Refs.^{20,29,30}.

IV. RESULTS AND DISCUSSION

A. Electronic and lattice contribution

For all compounds, the total specific heat C_{tot} was analyzed as a sum of an electronic C_e , a phonon C_{ph} , a nuclear C_N , and a magnetic contribution C_{mag} :

$$C_{tot} = C_e + C_{ph} + C_n + C_{mag} \quad (12)$$

For consistency reasons, the lattice contribution was estimated from the specific heat of the isomorphous single-crystal of $\text{YNi}_2\text{B}_2\text{C}$.²⁹ We tried other means of estimating the phonon contribution (such as mass normalization³¹ or using other nonmagnetic isomorphs^{29,32}). It is found out that the spin-wave fit-parameters based on different methods are differing by only a few percent; other than this variation, the use of different estimation process does not influence the conclusions drawn from this work.

The low-temperature, normal-state electronic contribution of these compounds was evaluated from $C_{tot}(T, H)$ of $\text{YNi}_2\text{B}_2\text{C}$ single-crystal (the same as that used in Ref.²⁹). Within the normal state (or $H > H_{c2}$ if applicable), the electronic, phonic, or nuclear contributions are taken to be field independent (see below). An illustration of the various contributions of $R\text{Ni}_2\text{B}_2\text{C}$ ($R = \text{Ho, Er}$) are shown in Fig. 1; evidently for all $R = \text{Gd, Ho, Er}$ compounds, the diamagnetic contribution is small in comparison with the magnetic or nuclear term.

B. Nuclear Contribution

The magnetic contribution was obtained as follows: after subtracting the electronic and phonon by the process explained in §IV.A, the resultant ($C_{tot} - C_e - C_{ph}$) is confronted with the sum of the nuclear (Eq. 13) and magnetic (Eq. 8) terms. Finally, the magnetic

FIG. 1: (Color online) Log-log plot of the zero-field $C_{tot}(T)$ versus T showing the various individual contributions that are contained in Eq. 12: (a) HoNi₂B₂C and (b) ErNi₂B₂C. The triangles (circles) denote the experimental total (magnetic) specific heats, while the lines represent the various calculated contributions: dotted, dashed, solid-thin (red) and solid-thick (black) lines represent, respectively, the electron+phonon, nuclear, magnetic, and total contribution. Both nuclear and magnetic contributions are obtained from the least-square fits (see text).

contribution is obtained after subtracting out the nuclear specific heat term which is usually given as:^{33,34}

$$C_n(T) = \Lambda_{iso} \left(\sum_{i=-I}^{+I} \sum_{j=-I}^{+I} (\omega_j^2 - \omega_i \omega_j) \exp\left(\frac{-\omega_j - \omega_i}{k_B T}\right) \right) / \left[\sum_{i=-I}^{+I} \sum_{j=-I}^{+I} \exp\left(\frac{-\omega_j - \omega_i}{k_B T}\right) \right],$$

$$\omega_i = (\alpha_{int} + \alpha_{ext}) \cdot i - P \cdot \left(i^2 - \frac{I(I+1)}{3} \right) \quad (13)$$

where Λ_{iso} is the isotope abundance, α_{int} and P are the magnetic dipole and electric quadrupole interaction parameters of the nuclear spins, respectively; I is the total nuclear spin while i is its component along the quantization axis. α_{ext} is associated with the externally applied magnetic field which is extremely small if compared to the internal field: for, say, $\text{ErNi}_2\text{B}_2\text{C}$,³⁴ $H_{int} \approx 7 \times 10^6$ Oe and thus the highest applied field is only $\sim 1\%$ of H_{int} .

TABLE I: The nuclear hyperfine parameters (Λ_{iso} , α_{int} , and P) and the spin-wave parameters (Δ_a and D_a) of $\text{HoNi}_2\text{B}_2\text{C}$ and $\text{ErNi}_2\text{B}_2\text{C}$ which are obtained after fitting the experimental ($C_{tot} - C_e - C_{ph}$) curves to the sum of the nuclear (Eq. 13) and magnetic (Eq. 8) terms. The specified temperature range indicates the region wherein the nuclear contribution is dominant (for the temperature range of the fit see § IV.C.2 and § IVC.3). The obtained nuclear parameters are compared with the corresponding parameters of the R -metal (see text).

$R\text{Ni}_2\text{B}_2\text{C}$	Temp. range	Λ_{iso}	I	α_{int}	P	Δ	D
	(K)	%		K	mK	K	K
$\text{HoNi}_2\text{B}_2\text{C}$	[0.5,1.5]	100	7/2	0.362	-9.6	7.7 ± 0.3	4.6 ± 0.2
Ho metal ³³	[0.03,0.5]	100	7/2	0.32	7.0		
$\text{ErNi}_2\text{B}_2\text{C}$	[0.1,0.5]	90(5)	7/2	0.054	2.9	7.0 ± 0.1	3.0 ± 0.1
Er metal ³⁴	[0.03,0.8]	100	7/2	0.042	-2.7		

The least square fit involves the simultaneous search for the best values of the five parameters, namely the nuclear parameters Λ_{iso} , α_{int} , and P as well as the spin-wave parameters Δ_a and D_a (see below). After the substitution of the obtained nuclear parameters (Table I), the expression of $C_n(T)$ (see Eq. 13) does reproduce satisfactorily the measured nuclear specific heat of $\text{ErNi}_2\text{B}_2\text{C}$ and $\text{HoNi}_2\text{B}_2\text{C}$ ($\text{GdNi}_2\text{B}_2\text{C}$ has no nuclear contribution): the overall fits are shown in Fig. 1. It is evident that α_{int} of the studied R^{3+} compounds are close to the values reported for the corresponding rare-earth metals^{33,34} indicating that the hyperfine field is determined mainly by the internal electronic configuration of the R^{3+} ion. On the other hand, the P parameters are extremely small; this is not surprising since the point group of the sites at which the R^{3+} nucleus resides is D_{4h} in borocarbides and D_{6h} in the elemental rare earth.

C. Magnetic contribution

Based on the general features of the $C_{mag}(T, H)$ curves (shown in Figs. 2, 5, and 7), one distinguishes four temperature regions: (i) a paramagnetic region, $T > T_N(H)$, wherein $C_{mag}(T, H)$ is due to change in the population of the crystal field levels, (ii) a critical region, $T \approx T_N(H)$, wherein $C_{mag}(T, H)$ is related to critical phenomena, (iii) an intermediate region, $T_X < T < T_N$ ($T_X = T_R$ for $\text{GdNi}_2\text{B}_2\text{C}$ or T_{WFM} for $\text{ErNi}_2\text{B}_2\text{C}$) which encompasses the sine modulated states. Within this region, the spin-wave analysis of § II.A.1-2 is not applicable. Finally (iv) the low-temperature region which should be restricted if one intends to analyze $C_{mag}(T, H_{\parallel\theta})$ in terms of the linearized magnon theory: below we restrict this range to $T < \Delta$ and $H < H_{sf}$ (none of the compounds under study presents the $H > H_{sat}$ case). Within this region, the collinear AFM/squared-up states are established and the measured $C_{mag}(T, H)$ is to be confronted with Eq. 8. It is worth mentioning that for extremely low-temperatures ($T \ll \Delta$), the exponential decaying character of $C_{mag}(T, H)$ (see Eq. 10) and the relatively large contribution of the nuclear Schottky contribution limit the usefulness of the lower temperature range for the magnon analysis.

1. $\text{GdNi}_2\text{B}_2\text{C}$

The zero-field magnetic structure of $\text{GdNi}_2\text{B}_2\text{C}$ ($T_N = 19.5$ K) is an incommensurate sine-modulated structure (moments along b axis and $\vec{q} = 0.551a^*$).^{27,35,36} At $T_R \approx 13.5$ K, a moment reorientation sets-in leading to an additional modulated mode transversely polarized and having a small amplitude along the c -axis.^{35,36} Two $H - T$ phase diagrams were reported:²³ one for $H \parallel a$ and another for $H \parallel c$. The phase diagram for $H \parallel a$ shows three field-induced magnetic phase transitions [see inset of Fig.2 (a)]: (i) the saturation boundary with H_{sat} ; (ii) the reorientation boundary $H_R^{\parallel a}$; and finally (iii) the domain-wall boundary $H_D^{\parallel a}$. In contrast, the phase diagram for $H \parallel c$ shows only two transitions [see inset of Fig.2 (b)]: $H_{sat}^{\parallel c}$ and $H_R^{\parallel c}$; in comparison, the thermal evolution of the former (latter) is similar to (different from) that of $H_{sat}^{\parallel a}$ ($H_R^{\parallel a}$). None of the two phase diagrams shows those characteristic H -induced cascade of metamagnetic phase transitions which are common in, say, the case of $R = \text{Er}, \text{Ho}$; this is attributed to the absence of strong anisotropic features.

As mentioned above, the experimental magnetic specific heat of $\text{GdNi}_2\text{B}_2\text{C}$ would be

confronted with two model calculations: (i) the magnon calculation which is valid for sub-helium temperature (§ II.A) and the model calculations of Jensen and Rotter⁸ which are extended from the helium-temperature range up to T_N (§ II.B).

FIG. 2: (Color online) The isofield $C_{mag}(T, H)$ of GdNi₂B₂C at various magnetic fields applied along (a) $H\|a$ and (b) $H\|c$. The inset at the bottom-left (top-left) illustrates the $H - T$ phase diagram for $H\|a$ ($H\|c$);²³ there, the horizontal dotted lines represent the fields that were applied during these measurements. Evidently, both $H_R^{\|c}$ and $H_R^{\|a}$ anomalies in the $C_{mag}(T, H)$ curve do reproduce the boundaries of the phase diagrams, in particular the reentrant feature appearing for the $H\|a$ case (see text).

a. Magnon contribution to $C_{mag}(T, H)$ Figure 2 shows that the most prominent features of $C_{mag}(T, H)$ of GdNi₂B₂C are (i) the characteristic and distinct evolution of the $H_{sat}(T)$ and $H_R(T)$ curves and that (ii) within a certain region of T and H , $C_{mag}(T, H)$ appears to be hardly influence by H . The cause of this apparent collapse of the $C_{mag}(T, H)$ curves becomes clear if we compare these curves with the predictions of Eq. 8: Fig. 3

shows a fit of the measured $C_{mag}(T, H = 0)$ curve to Eq. 8 and the obtained fit parameters are $\Delta = 2.9 \pm 0.1$ K and $D = 5.6 \pm 0.1$ K which are close but, due to the difference in the temperature range, are better than those reported in Ref.²⁰. As both Δ_a and D_a are field independent, then the insertion of these values into Eq. 8 leads to the calculated $C_{mag}(T, H)$ curves (with no adjustable parameters) for all fields up to $H < k_B \Delta_a / (g \mu_B) \sim 20$ kOe which is the field above or equal to which the magnon calculations based on Eq. 8 are not valid. Evidently the calculated and measured curves collapse on each other when T/Δ_a is in the immediate neighborhood of 1: thus the apparent collapse is a reminder that our experimental conditions are good only for probing that part of the phase diagram wherein the field has a weak influence on the strongly exchanged-coupled AFM-like state. It is worth mentioning that such a collapsing feature is reflected also, by virtue of Eq. 11b, in the low-temperature $M(T, H)$ curves.^{23,27}

Figure 2 shows also that the H -evolution of the low-temperature $C_{mag}(T, H_{\parallel c})$ curves is similar to that of $C_{mag}(T, H_{\parallel a})$ ones; the only difference is that all values of $H_{\parallel a}$ are lower than $H_R^{\parallel a}(T < T_R)$ boundary while, in contrast, some of the applied $H_{\parallel c}$ values are higher than $H_R^{\parallel c}(T < T_R)$ (see above); then it is no surprise that the presence of the $T_R(H_{\parallel c})$ -event in $C_{mag}(T, H_{\parallel c})$ is more pronounced than in $C_{mag}(T, H_{\parallel a})$; in fact there is no manifestation of the reorientation event in the isofield $C_{mag}(T, H_{\parallel c} > 32$ kOe) curves while, in contrast, for $H_{\parallel a}$, the presence of the reorientation event is evident in all applied field up to the maximum 80 kOe (see insets of Fig. 2). It is noted that the reentrant feature of the $H_R^{\parallel a}(T)$ curve within the neighborhood of 11 K is well evident in the $C_{mag}(T, H_{\parallel a})$ curves: as $H_{\parallel a}$ is increased, the peak associated with this event moves first to higher temperature but reverts to a decreasing tendency when $H_{\parallel a}$ reaches values higher than 30 kOe.

Within $T < 5$ K and $H_{\parallel a} < H_R(T)$ range, $(\partial S_{mag}/\partial H)_T$, $(\partial C_{mag}/\partial H)_T$, and $(\partial M/\partial T)_H$ [Ref.^{23,27}] are weak but positive. Similar features are evident for the $H_{\parallel c}$ case. When $H_{\parallel c} \rightarrow H_R(T)$, $C_{mag}(T, H_{\parallel c})$ is observed to increase, reaching a maximum at the phase boundary. A further increase in $H_{\parallel c} > H_R(T < T_R)$ leads to $(\partial C_{mag}/\partial H)_T < 0$ indicating a decrease in the entropy and as such an increase in the ordered component along the c axis. For $T > T_R$, both $(\partial M/\partial T)_H$ [Refs.^{23,27}] and $(\partial C_{mag}/\partial H)_T$ are weak and positive for $H < 30$ kOe but negative for $30 \text{ kOe} < H < H_{sat}$.

b. Model calculation of $C_{mag}(T, H)$ Figure 4 compares the measured magnetic specific heat of $\text{GdNi}_2\text{B}_2\text{C}$ with the model calculation of Jensen and Rotter (see § II.B).⁸ It is assuring

FIG. 3: (Color online) Log-Log plot of C_{mag} versus the normalized temperature (T/Δ) under different applied fields. Δ_a represent the zero-field energy gap of Eq. 7. Symbols denote measurements while solid lines represent the calculated $C_{mag}(T, H)$ based on Eq. 8. The zero-field $C_{mag}(T, H)$ curve (measured down to 0.5 K) was fitted with Eq. 8. The obtained parameters were fed into Eq. 8 and there from the theoretical $C_{mag}(T, H)$ curves for field up to 20 kOe were calculated with no adjustable parameters (see text).

to notice that, even though there are no adjustable parameters in these calculations, the model is able to reproduce the main features of the measured $C_{mag}(2 \text{ K} < T < T_N)$ for both $H_{\parallel a} \leq 80 \text{ kOe}$ and $H_{\parallel c} \leq 80 \text{ kOe}$ [see, respectively, Figs. 4(a) and (b)]. The following three achievements of the model calculations should be highlighted: (i) the calculated magnitude of the steps at both T_R and T_N compare favorably with the measured values; (ii) the surge of an anisotropy for the *spherical* $7/2S$ Gd-moments even at temperatures as high as 20 K is well accounted for; and (iii) the reorientation process at T_R (along both field orientations) is shown to be a consequence of the joint action of exchange interactions and dipolar forces even

FIG. 4: Comparison of the calculated (solid lines) and measured (symbol) field-dependent magnetic specific heat of $\text{GdNi}_2\text{B}_2\text{C}$ for (a) $H\parallel a$ axis and (b) $H\parallel c$ axis. For ease of visualization, the successive curves are displaced upwards with the same amount of vertical shift (10 J/moleK). The calculations (with no adjustable parameters) are based on the model proposed by Jensen and Rotter⁸ (see text).

though the energy of the former is at least five times larger than that of the latter: isotropic bilinear interaction, alone by themselves, do not lead to any reorientation processes.^{31,37,38} Evidently in spite of the above-mentioned successes, this mean-field model calculation are not expected to account for the magnetic features of the specific heat within the very low-temperatures or in the neighborhood of T_N (the critical region).

2. $\text{HoNi}_2\text{B}_2\text{C}$

The zero-field magnetic ground structure of $\text{HoNi}_2\text{B}_2\text{C}$ is an AFM state wherein the ferromagnetic basal planes are piled along the c axis forming an AFM configuration $\nearrow\swarrow$ with $q = (0,0,1)$.³⁹ On applying a field along the easy $(1,1,0)$ axis, the phase diagram of $\text{HoNi}_2\text{B}_2\text{C}$ shows a succession of field-induced metamagnetic phases,^{11,12,40} transforming from $\nearrow\swarrow$ into: $\nearrow\swarrow$ at H_1 , $\nearrow\searrow$ at H_2 , and a saturated $\nearrow\nearrow$ state at H_{sat} . On the other hand, if the field is applied within the ab plane but at an angle θ away from the easy axis, then the strong CEF-induced anisotropic character of $\text{HoNi}_2\text{B}_2\text{C}$ becomes evident and as a result restricts the moments to be along only the $\langle 110 \rangle$ directions: as shown in the lower inset of Fig. 5, an increase in θ induces an increase in both H_1 [expressed as $4.1/\cos(\theta)$ kOe] and H_{sat} [related by $6.6/\sin(45-\theta)$ kOe] but a decrease in H_2 [described by $8.4/\cos(45-\theta)$ kOe].¹⁵

Figure 5 shows the thermal evolution of the isofield $C_{mag}(T, H)$ of $\text{HoNi}_2\text{B}_2\text{C}$ for various fields, all applied along the (100) axis ($\theta=45^\circ$); its overall field-dependence can be comprehended in the light of Eq. 11b, the $M(T, H)$ curves, and the features of the magnetic phase diagrams. One of the most remarkable features of these $C_{mag}(T, H)$ curves is the observation that their field-dependence (the upper inset of Fig. 5) is reminiscent of the field-dependence of the isothermal $M(T, H)$: as an example, for $H \leq H_1$,¹³ $(\partial^2 M/\partial^2 T)_H > 0$ and concomitantly $C_{mag}(T, H)$ (see Fig. 5) increases with H . Furthermore, $C_{mag}(T, H_1 < H < H_2)$ is relatively much higher but $C_{mag}(T, H > H_2)$ decreases monotonically with the field as it approaches the forced saturated $\nearrow\nearrow$ state.

Based on the $H-\theta$ phase diagram (lower inset of Fig. 5), it becomes clear that among the various $C_{mag}(T, H)$ curves, the only candidates to be contrasted with the spin wave analysis of § II.A.1 are those measured within the $H < H_1$ range, namely $H_{\parallel a} = 0$ and 2.5 kOe wherein the low- T collinear AFM $\nearrow\swarrow$ state is established.¹⁵ Fig. 6 shows the satisfactorily fit of $C_{mag}(T, H = 0)$ and the best fit parameters are: $\Delta = 7.7 \pm 0.3$ K and $D = 4.6 \pm 0.2$ K. These values are in agreement with our earlier results.³⁰ Based on Eq. 8, the thermal evolution of the $C_{mag}(T, H_{\parallel a} = 2.5$ kOe) should be obtainable from these Δ and D and the value of the field component along the (110) direction; this is indeed the case as can be convincingly observed in Fig. 6.

FIG. 5: (Color online) Thermal evolution of the magnetic specific heats of $\text{HoNi}_2\text{B}_2\text{C}$ under various applied fields.³⁰ For clarity, the $C_{mag}(T, H \leq 10 \text{ kOe})$ curves are plotted in the lower panel while the $C_{mag}(T, H \geq 10 \text{ kOe})$ curves are plotted in the upper panel. The lower inset shows the angular dependence of the critical fields (adapted from Ref.¹⁵); the horizontal dashed lines represent the applied fields. The upper inset shows the field-dependence of the magnetic specific heat at 2 K: $C_{mag}(T, H)$ within the same metamagnetic state is almost the same; this feature is reflected also in the $M(2K, H)$ isotherms reported in Ref.¹⁵ (see text).

3. $\text{ErNi}_2\text{B}_2\text{C}$

The magnetic phase diagram of $\text{ErNi}_2\text{B}_2\text{C}$ is shown in the inset of Fig. 7:¹⁶ in zero field, this compound superconducts at 10.5 K and orders magnetically at $T_N = 6.4 \text{ K}$ into an incommensurate modulated AFM structure with $q=(0.55,0,0)$ and moments pointing along the b axis.³⁹ Below $T_{WFM} = 2.2 \text{ K}$, a weak ferromagnetic (WFM) state¹⁴ emerges together with an equal-amplitude, squared-up state.^{41,42} A series of field-induced metamagnetic trans-

FIG. 6: (Color online) A log-log plot of the isothermal $C_{mag}(T/\Delta_a, H)$ curves of $\text{HoNi}_2\text{B}_2\text{C}$. Δ_a represent the zero-field energy gap of Eq. 7. For clarity, the $C_{mag}(T/\Delta_a, H \leq 10 \text{ kOe})$ curves are plotted in the lower panel while those of $C_{mag}(T/\Delta_a, H \geq 10 \text{ kOe})$ curves are plotted in the upper panel. The solid line represents the non-linear least square fit of the zero-field measured curve to Eq. 8 (see text).

formations appears when a field ($H < H_{sat}$) is applied along the easy axis $(0,1,0)$:^{10,16,17,40} at 2 K, three metamagnetic transformations occur at 4, 11, and 20 kOe. For $H > H_{sat}$, the paramagnetic saturated state is stabilized.

To investigate the H - and T -dependence of $C_{mag}(T, H)$ across such a phase diagram, we carried out a series of isofield measurements with $H \parallel (010)$. The resulting $C_{mag}(T, H_{\parallel a})$ curves are shown in Figs. 7. The thermal evolution of the zero-field entropy (not shown) suggests that the lowest four level are fully populated above 10 K; this result is in agreement with the findings of Gasser *et al.*⁴³ that the electronic ground state is a doublet which is

FIG. 7: (Color online) Thermal evolution of $C_{mag}(T, H)$ of $\text{ErNi}_2\text{B}_2\text{C}$ at various magnetic fields. The inset shows the $H - T$ phase diagram (adapted from Ref.¹⁶): the thick dashed line represent the $H_{c2}(T)$ –superconductivity– curve while the solid lines represent the various magnetic transformations. The horizontal dotted lines represent the magnetic fields that were used during this study.

separated from the immediate excited state (also a doublet) by $0.6 \sim 0.7$ meV ($7 \sim 8$ K). For $H < H_1$ ($T < T_{WFM}$), an increase in H induces an increase in $S_{mag}(H)$ and, based on Eq. 11a and the experimental results,²⁶ $(\partial M / \partial T)_H > 0$ (considerations should be made for the presence of the superconductivity below H_{c2} and the surge of weak ferromagnetic state below T_{WFM}).

For $T < T_{WFM}$ ($H < H_1$), the zero-field magnetic state is approximated as an AFM structure (see § II.A); accordingly, the measured $C_{mag}(T < T_{WFM}, H < H_1)$ curves are confronted with Eq. 8. Fig. 8 shows the excellent fit of $C_{mag}(T, H = 0 \text{ kOe})$ which gives

FIG. 8: (Color online) A log-log plot of the $C_M(T, H)$ curves of $\text{ErNi}_2\text{B}_2\text{C}$ at various applied magnetic fields. The magnetic specific heat (symbol) are compared with the theoretical calculation (lines) based on Eq. 8 (see text). The calculated curves of $H=0, 5, 10$ kOe are different from each other only at $T < \Delta$.

$\Delta = 7.0 \pm 0.1$ K and $D = 3.0 \pm 0.1$ K. Using these parameters, we calculated the field-dependent $C_{mag}(T, H)$ curves (see Fig. 8). Once more, one observes the collapse of the $C_{mag}(T < T_{WFM}, H < H_1)$ curves within the immediate neighborhood of T_{WFM}^- . Due to experimental limitations, we were not able to probe the field evolution for $T < T_{WFM}$ nor the thermal evolution for $H > H_{sat}$ of $C_{mag}(T, H)$ of $\text{ErNi}_2\text{B}_2\text{C}$.

V. DISCUSSION AND SUMMARY

The general evolution of $C_{mag}(T, H)$ within the magnetically ordered state of representative RNi_2B_2C ($R=Gd, Ho, Er$) is found to reflect faithfully the characteristic features of their $H-T$ phase diagrams. Three approaches are employed for the analysis of the evolution of these $C_{mag}(T, H)$ curves: (i) basic thermodynamical analysis which allows us to relate the evolution of $C_{mag}(T, H)$ to that of the magnetization measurements: thus permitting a generalization to field and temperature ranges beyond the limitation of our experimental set ups. (ii) the linearized spin-wave analysis which allows us to investigate the low-temperature, low-field range; and (iii) the model calculation based on which we are able to probe the higher temperature region, a region which is not accessible for spin-wave analysis.

One of the characteristic features of the magnetic phase diagrams is the stair-like behavior observed in the magnetization isotherms: it is assuring that this feature is manifested also in the $C_{mag}(T, H)$ case: all the $C_{mag}(T, H)$ curves within the same metamagnetic mode do collapse on each other (see e.g. Fig. 5). This feature is related to the influence of the elementary magnetic excitations on the thermodynamical properties and here, in this work, we discuss this influence in terms of the linearized spin-wave model (see the theory in § II.A and its confrontation with the measured $C_{mag}(T, H)$ curves in § IV.C)

Based on the analysis of § IV one is able to delineate the low-field, low-temperature range of the $H-T$ phase diagrams wherein the linearized magnon contribution is found to describe satisfactorily the experimental results: for $GdNi_2B_2C$, it is the $H < H_R(T)$ range wherein the sine-modulated state is squared-up; for $ErNi_2B_2C$ it encompasses the $H < H_1(T < T_{WFM})$ range wherein the squared-up AFM-like state is established; and finally for $HoNi_2B_2C$, it is the $H < H_1 (T < T_N)$ range wherein the collinear AFM structure is established. In all these magnetic states, the dispersion relation is taken to be given by Eq. 6 and the magnetic specific heat is expressed by Eq. 8: the satisfactory agreements between the calculated and measured $C_{mag}(T, H)$ justifies the assumptions considered in this model.

The values of the fit parameters evolves reasonably well across the studied compounds: as an example, the gap parameter of $GdNi_2B_2C$ ($\Delta = 2.9$ K) is much smaller than the corresponding values of $HoNi_2B_2C$ ($\Delta = 7.7$ K) and $ErNi_2B_2C$ ($\Delta = 7.0$ K); based on Eq. 7, such a result does agree with the well-established fact that the anisotropic field for $GdNi_2B_2C$ is extremely small. On the other hand, the stiffness constant of $GdNi_2B_2C$

($D = 5.5$ K) is greater than that of $\text{HoNi}_2\text{B}_2\text{C}$ ($D = 4.6$ K) and $\text{ErNi}_2\text{B}_2\text{C}$ ($D = 3.0$ K); based on Eq. 9, this is related to the fact that the effective exchange couplings of $\text{GdNi}_2\text{B}_2\text{C}$ (proportional to the de Gennes factor) are the strongest. It is recalled that no direct scaling with the de Gennes factor should be expected since the D term of Eq. 9 contains also H_a .

As the investigated compounds are good representatives of the other magnetic borocarbides, then it is expected that the above mentioned characteristic step-like behavior should be manifested also in other magnetic $R\text{Ni}_2\text{B}_2\text{C}$ compounds: indeed, the $M(T, H)$ isotherms of $\text{TbNi}_2\text{B}_2\text{C}$ (having similar anisotropic features as those of $\text{ErNi}_2\text{B}_2\text{C}$) manifest such a stair-like feature.^{40,44,45} Then, based on Eq. 11b, its $C_{mag}(T, H)$ features should be similar to the those of the studied compounds. It is emphasized that the manifestation of such stair-like features is a more general property since it is manifested, not only in the $M(T, H)$ isotherms, but also in several other thermodynamical quantities (see § II.B). This generality suggests that, although other models have been applied to analyze these stair-like features in, e.g., $\text{HoNi}_2\text{B}_2\text{C}$ [Ref.^{4,5}] and $\text{ErNi}_2\text{B}_2\text{C}$,⁶ an analysis in terms of the spin-wave model is shown to be extremely useful for the description of the low-temperature thermodynamical properties of these magnetic compounds.

Acknowledgments

We acknowledge the partial financial support from the Brazilian agencies CNPq (485058/2006-5) and Faperj (E-26/171.343/2005) and the Austrian Science Foundation (FWF) P16250.

-
- ¹ K.-H. Müller and V. N. Narozhnyi, Rep. Prog. Phys. **64**, 943 (2001).
 - ² P. C. Canfield, P. L. Gammel, and D. J. Bishop, Phys. Today **51**, 40 (1998).
 - ³ B. K. Cho, P. C. Canfield, and D. C. Johnston, Phys. Rev. Lett. **77**, 163 (1996).
 - ⁴ V. A. Kalatsky and V. L. Pokrovsky, Phys. Rev. B **57**, 5485 (1998).
 - ⁵ A. Amici and P. Thalmeier, Phys. Rev. B **57**, 10 684 (1998).
 - ⁶ J. Jensen, Phys. Rev. B **65**, 140514(R) (2002).
 - ⁷ M. Rotter, A. Schneidewind, M. Doerr, M. Loewenhaupt, M. El Massalami, and C. Detlefs, Physica B **345**, 231 (2004).

- ⁸ J. Jensen and M. Rotter, Phys. Rev. B **77**, 134408 (2008).
- ⁹ J. W. Lynn, S. Skanthakumar, Q. Huang, S. K. Sinha, Z. Hossain, L. C. Gupta, R. Nagarajan, and C. Godart, Phys. Rev. B **55**, 6584 (1997).
- ¹⁰ A. J. Campbell, D. McK. Paul, and G. J. MacIntyre, Solid State Comm. **115**, 213 (2000).
- ¹¹ A. J. Campbell, D. McK. Paul, and G. J. MacIntyre, Phys. Rev. B **61**, 5872 (2000).
- ¹² C. Detlefs, F. Bourdarot, P. Burlet, P. Dervenagas, S. L. Bud'ko, and P. C. Canfield, Phys. Rev. B **61**, 14 916 (2000).
- ¹³ P. C. Canfield, B. K. Cho, D. C. Johnston, D. K. Finnemore, and M. F. Hundley, Physica C **230**, 397 (1994).
- ¹⁴ P. C. Canfield, S. L. Bud'ko, and B. K. Cho, Physica C **262**, 249 (1996).
- ¹⁵ P. C. Canfield, S. L. Bud'ko, B. K. Cho, A. Lacerda, D. Farrell, E. Johnston-Halperin, V. A. Kalatsky, and V. L. Pokrovsky, Phys. Rev. B **55**, 970 (1997).
- ¹⁶ S. L. Bud'ko and P. C. Canfield, Phys. Rev. B **61**, R14 932 (2000).
- ¹⁷ M. Doerr, M. Rotter, M. El Massalami, S. Sinning, H. Takeya, and M. Loewenhaupt, J. Phys.: Condens. Matter **14**, 5609 (2002).
- ¹⁸ C. Kittel, *Quantum Theory of Solids* (John Wiley and Sons Inc., New York, 1963).
- ¹⁹ R. J. Joenk, Phys. Rev. **128**, 1634 (1962).
- ²⁰ M. El Massalami, R. E. Rapp, F. A. B. Chaves, H. Takeya, and C. M. Chaves, Phys. Rev. B **67**, 224407 (2003).
- ²¹ M. Rotter, A. Lindbaum, A. Barcza, M. El Massalami, M. Doerr, M. Loewenhaupt, M. Michor, and B. Beuneu, Europhys. Lett. **75**, 160 (2006).
- ²² M. Rotter, J. Mag. Magn. Mat. **272-276**, 481 (2004).
- ²³ M. El Massalami, H. Takeya, K. Hirata, M. Amara, R.-M. Galera, and D. Schmitt, Phys. Rev. B **67**, 144 421 (2003).
- ²⁴ M. El Massalami and E. Baggio-Saitovitch, J. Magn. Magn. Mater. **153**, 97 (1996).
- ²⁵ I. R. Fisher and et al, Phys. Rev. B **56**, 10 820 (1997).
- ²⁶ B. K. Cho, P. C. Canfield, L. L. Miller, D. C. Johnston, W. P. Beyermann, and A. Yatskar, Phys. Rev. B **52**, 3684 (1995).
- ²⁷ P. C. Canfield, B. K. Cho, and D. C. Johnston, Physica B **215**, 337 (1995).
- ²⁸ H. Takeya, T. Hirano, and K. Kadowaki, Physica C **256**, 220 (1996).
- ²⁹ M. El Massalami, R. E. Rapp, and H. Takeya, in *Studies in High Temperature Superconductors*,

edited by A. Narlikar (Nova Science, New York, 2003), vol. 45.

- ³⁰ M. El Massalami, H. Takeya, and C. M. Chaves, Phys. Rev. B **70**, 014429 (2004).
- ³¹ M. Bouvier, P. Lethuillier, and D. Schmitt, Phys. Rev. B **43**, 13137 (1991).
- ³² H. Michor, T. Holubar, C. Dusek, and G. Hilscher, Phys. Rev. B **52**, 16 165 (1995).
- ³³ M. Kruis, G. R. Pickett, and M. C. Veuro, Phys. Rev. B **177**, 910 (1969).
- ³⁴ M. Kruis, G. R. Pickett, and M. C. Veuro, Solid State Commun. **14**, 191 (1974).
- ³⁵ C. Detlefs, A. I. Goldman, C. Stassis, P. C. Canfield, B. K. Cho, J. Hill, and D. Gibbs, Phys. Rev. B **53**, 6355 (1996).
- ³⁶ K. Tomala, J. P. Sanchez, P. Vulliet, P. C. Canfield, Z. Drzazga, and A. Winiarska, Phys. Rev. B **58**, 8534 (1998).
- ³⁷ J. A. Blanco, D. Gignoux, and D. Schmitt, Phys. Rev. B **43**, 13145 (1991).
- ³⁸ M. Rotter, M. Loewenhaupt, M. Doerr, A. Lindbaum, and H. Michor, Phys. Rev. B **64**, 014402 (2001).
- ³⁹ J. W. Lynn, S. Skanthakumar, Q. Huang, S. K. Sinha, Z. Hossain, L. C. Gupta, R. Nagarajan, and C. Godart, Phys. Rev. B **55**, 6584 (1997).
- ⁴⁰ P. Canfield and S. Bud'ko, J. Alloys Compounds **262-263**, 169 (1997).
- ⁴¹ H. Kawano-Furukawa, H. Takeshita, M. Ochiai, T. Nagata, H. Yoshizawa, N. Furukawa, H. Takeya, and K. Kadowaki, Phys. Rev. B **65**, 180508(R) (2002).
- ⁴² S.-M. Choi, J. W. Lynn, D. Lopez, P. L. Gammel, P. C. Canfield, and S. L. Bud'ko, Phys. Rev. Lett. **87**, 107001 (2001).
- ⁴³ U. Gasser, P. Allenspach, F. Fauth, W. Henggeler, J. Mesot, A. Furrer, S. Rosenkranz, P. Vorderwisch, and M. Buchgeiste, Z. Phys. B **101**, 345 (1996).
- ⁴⁴ B. K. Cho, P. C. Canfield, and D. C. Johnston, Phys. Rev. B **53**, 8499 (1996).
- ⁴⁵ M. ElMassalami, M. Amara, R.-M. Galera, D. Schmitt, and H. Takeya, Phys. Rev. B **76**, 104410 (2007).

APPENDIX A: THE HIGH-FIELD LIMIT ($H > H_{sat}$)

For the induced FM state, we assume that the action of both the anisotropic field and exchange couplings is the similar to the case of the low-field limit (§ II.A) except that here the field is strong enough to overturn the antiparallel spins: all the spins are oriented along

the easy-axis directions; e.g. for the case of $\text{HoNi}_2\text{B}_2\text{C}$, it is one of the four $\langle 110 \rangle$ directions that is nearest to the field. In the long wave limit, the dispersion relation simplifies to:

$$\hbar\omega_k = \Delta_f + c_1(k_x^2 + k_y^2) - c_2k_z^2, \quad (\text{A1})$$

where, assuming a weaker orthorhombic distortion ($a \approx b$):

$$c_1 = 2Sa^2(\mathcal{J}_0 - \mathcal{J}_1)$$

$$c_2 = 2Sc^2\mathcal{J}_1,$$

and the energy gap ($k = 0$):

$$\Delta_f = 2g\mu_B H \cos(\theta) / k_B. \quad (\text{A2})$$

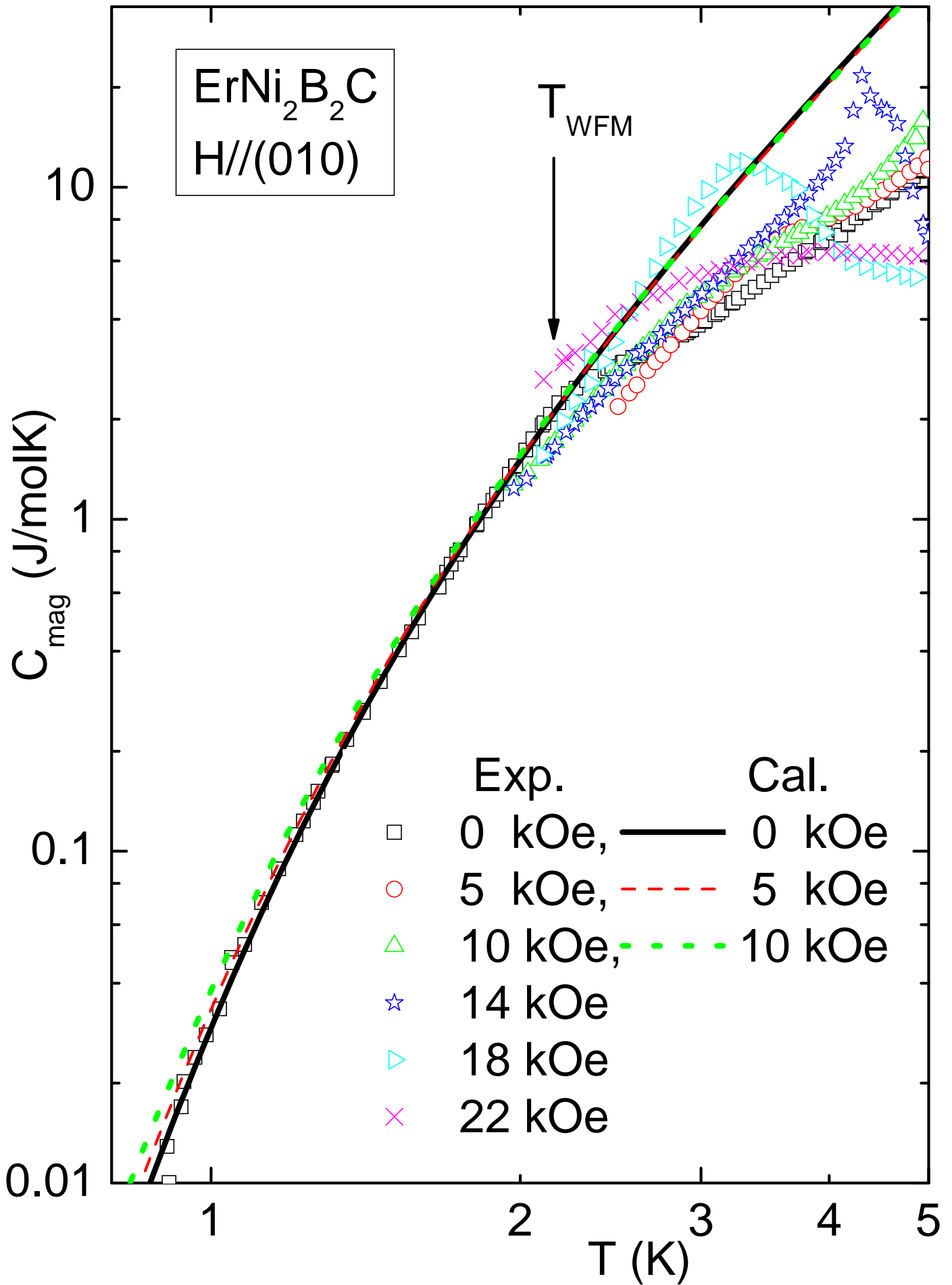
Thus, according to the above assumptions – involving the anisotropic field and exchange couplings – the spin-wave parameters of the saturated FM state are different from the standard (spontaneous) FM state: in the latter case the gap includes a $2H_a$ term and the sign of the c_2 term in Eq. A1 is positive. Applying standard procedure, the magnon contribution is given as:

$$C_{mag}(T) = \frac{R\Delta_f^{3/2}}{2^{3/2}\pi^2 D_f^{3/2} T} \sum_{m=1}^{\infty} [K_2(m\Delta_f/T)], \quad (\text{A3})$$

where

$$D_f = 2S(\mathcal{J}_0 - \mathcal{J}_1)^{\frac{2}{3}} \mathcal{J}_1^{\frac{1}{3}}. \quad (\text{A4})$$

For $T < \Delta_f$, Eq. A3 reduces to $R\Delta \exp(-\Delta/T)(\pi^{3/2} D_f^{3/2} T^{1/2})$ while for $T \gg \Delta_f$ it gives the well-known $T^{3/2}$ relation.¹⁸



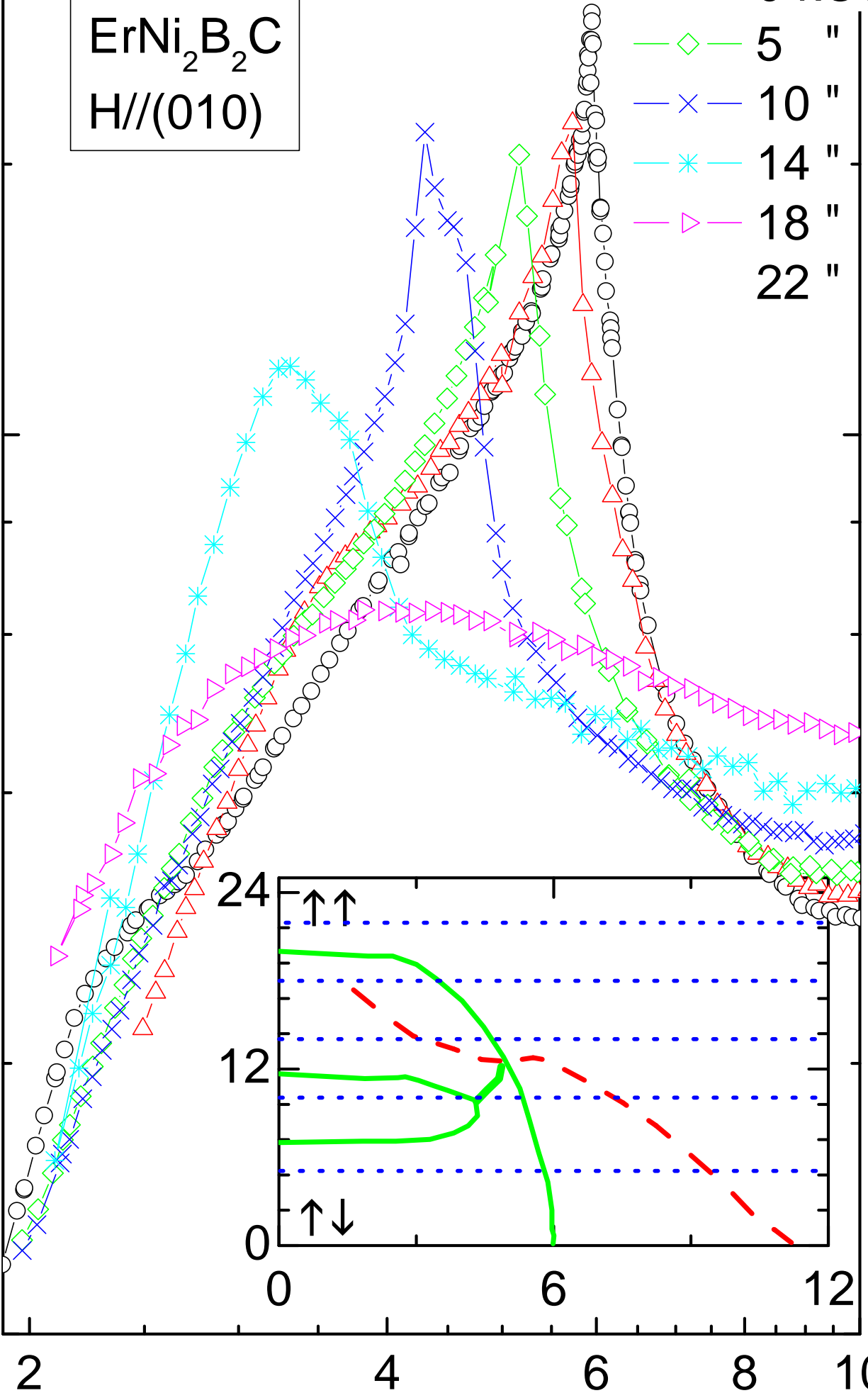
ErNi₂B₂C
H//(010)

- ◇— 5 "
- ×— 10 "
- *— 14 "
- ▷— 18 "
- 22 "

C_{mag} (J/molK)

10

1



T (K)

24

12

0

0

6

12

$\uparrow\uparrow$

$\uparrow\downarrow$

